A multi-analytical methodology for the characterization of industrial samples of spent Ni-MH battery powders

Margot Zielinski [a,b], Laurent Cassayre [a], Pascal Floquet [a], Mélina Macouin [c], Philippe Destrac [a], Nicolas Coppey [b], Cédric Foulet [b], Béatrice Biscans [a,*]

[a] Laboratoire de Génie Chimique, Université de Toulouse, CNRS, INPT, UPS, Toulouse, France
[b] Société Nouvelle d'Affinage des Métaux (S.N.A.M.), Viviez, France
[c] GET/OMP, UMR CNRS 5563, Université Paul-Sabatier, Toulouse, France

A multi-analytical methodology is implemented to characterize several sieving fractions of industrial samples of Black Mass (BM) powders originating from the thermo-mechanical treatment of cylindrical and prismatic-type spent nickel metal-hydride (Ni-MH) batteries. Elemental analyses of 17 elements (including C and O) indicate that the elemental composition of the powders (greater than93 %wt) does not depend on the battery type nor on the sieving fraction. XRD analyses evidence several phases (including Ni, NiO, CeO_2 and C) but their quantification is not possible. Beyond these standard characterisations, magnetic susceptibility measurements demonstrate that the amount of metallic nickel versus nickel oxide increases with the sieving fraction, and that powders from prismatic-type batteries contain twice as much metallic nickel than cylindrical ones. Thanks to statistical analysis (based on clustering algorithms) of an electron probe μ-analysis (EPMA) compositional map, the complete methodology allows us to propose a full phase distribution for the BM particles. Three types of particles are identified and quantified. They originate from the partial oxidation of the battery components (anode active mass, anode current collector, cathode active mass and cathode current collector). The whole picture highlights the joint importance of battery ageing mechanisms, thermal deactivation and BM sieving steps on powder composition.

1. Introduction

In Europe, the legislative framework of spent Ni-MH battery recycling has been defined by the 2006/66/EC directive, which sets a target recycling rate of over 50 %wt (ADEME, 2017). Ni-MH batteries can be separated into two main categories depending on their usage and fabrication methods. On the one hand, AA and AAA-type cylindrical batteries are used for portable consumer goods, often as single cells. They are collected from municipal waste systems; in such batteries, the electrodes are coiled into a bobbin and placed inside a protective steel casing (Bertuol et al., 2006). On the other hand, Ni-MH batteries that equip hybrid-electric vehicles (HEV) consist of cells that have a prismatic geometry where the electrode plates are stacked on each other. The whole assemblage is protected by a steel casing. In both cylindrical and prismatic batteries, the cathodes are usually composed of a metallic nickel mesh as the current collector, onto which particles of nickel hydroxide are deposited (Hall et al., 2014). The anodes consist of nickel-plated steel current collectors, onto which a hydride alloy is deposited containing light rare earth elements (La, Ce, Nd, Pr) and transition metals like Ni, Co, Mn and Al (Larsson et al., 2013). The electrodes are separated by a microporous polymer and alkaline electrolytes such as KOH are used (Al-thyabat et al., 2013).

Typical Ni-MH battery recycling processes consist of three main steps: collection and sorting of the different types of batteries, thermo-mechanical pre-treatment to transform the full batteries into powder, and hydrometallurgical treatment of the resulting powder aiming at a selective recovery of the valuable elements (mainly Ni and Co on the one side, and rare earth elements on the other side). The thermo-mechanical pre-treatment step is further detailed in Fig. 1. Due to their larger size and weight compared to cylindrical batteries, automotive batteries are manually dismantled prior to the battery deactivation step (Fig. 1) so as to recover the casing, printed circuit boards, copper cables and other electronic components (Wang and Friedrich, 2015). A thermal

* Corresponding author at: Laboratoire de Génie Chimique CNRS, 4 Allée Emile Monso CS 84234, 31432 Toulouse cedex 4, France.
E-mail address: beatrice.biscans@toulouse-inp.fr (B. Biscans).

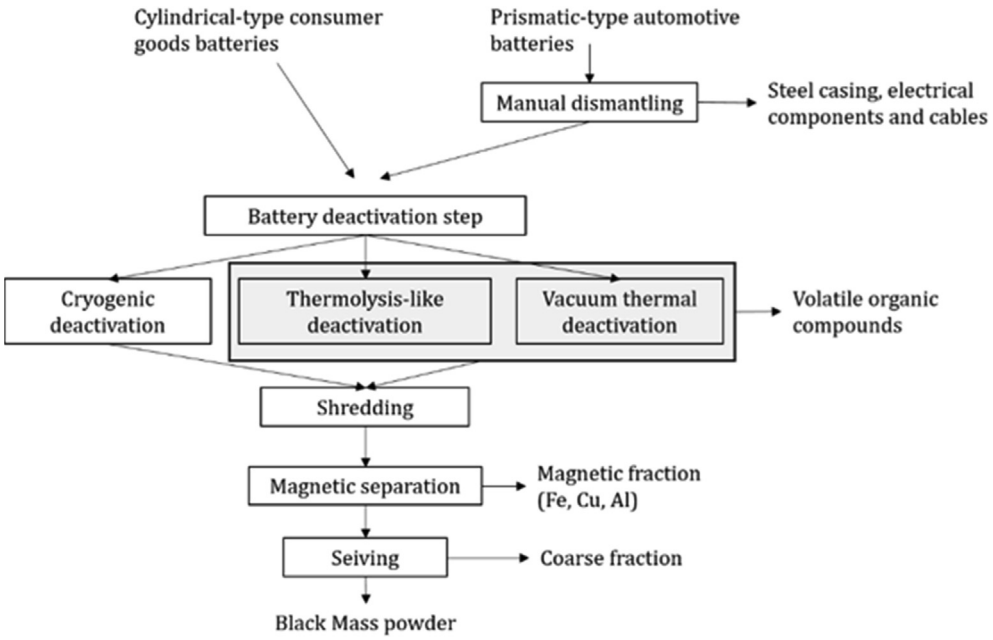

Fig. 1. Schematic of typical thermo-mechanical pre-treatment steps for Ni-MH battery recycling at industrial scale.

treatment is then carried out to fully discharge the batteries and facilitate their mechanical treatment. Several deactivation technologies exist (Fig. 1), such (i) as cryogenic deactivation that is being studied at the Institute of Non-Ferrous Metals (IMN) in Poland (Chmielarz and Becker, 2018) and implemented by Retrieve Technologies in the USA (Wang and Friedrich, 2015), (ii) vacuum thermal deactivation in a furnace as developed by ACCUREC Recycling GmbH in cooperation with Bayer Industries (Wang and Friedrich, 2015) and (iii) thermolysis-like thermal deactivation as performed at the Société Nouvelle d'Affinage des Métaux (SNAM) in France (Zielinski et al., 2020). As depicted in Fig. 1, once the batteries are discharged, hammer or knife milling can be applied, followed by magnetic separation. The strongly magnetic fraction is a Fe-alloy from the casing that can be recovered for secondary steel production. The weakly magnetic fraction is gradually sieved in order to obtain a powder enriched in valuable metals called Black Mass (BM), which will be used as the input material for hydrometallurgical processes.

In the recent literature concerning the pre-treatment of spent Ni-MH batteries, various research groups have studied the impact of milling and magnetic separation on the composition of BM powders (Al-thyabat et al., 2013; Bernardes et al., 2004; Bertuol et al., 2006; Crocce et al., 2004; Ebin et al., 2018; Huang et al., 2011; Innocenzi and Vegliò, 2012; Liu et al., 2019). In these works, phase identification is usually performed thanks to powder X-Ray diffraction (XRD) analysis. Global elemental distribution with respect to size classification is given thanks to mineralisation and Inductively Coupled Plasma – Optical Emission Spectroscopy (ICP-OES) analysis. However, apart in the recent study of Ebin et al. (2018), the carbon content in BM samples is rarely quantified; moreover, oxygen content has never been reported. As a result, it has been difficult to propose mass compositions of BM powders with mass balances higher than 70 %wt. Furthermore, powder XRD analyses do not allow to (i) identify the phases present in a specific type of particle and (ii) quantify the global proportions of the different phases in the sample powder. Nonetheless, from a hydrometallurgical process design and safety point of view, it is of high interest to know the proportions of the mineral phases and their attribution to respective types of particles for two main reasons. Firstly, the dissolution of the metallic elements contained in the BM powder using mineral acids leads to $H_{2(g)}$ outgassing (Larsson et al., 2013; Zielinski et al., 2020), which may cause a risk of explosion if the gas volume is not handled properly. Secondly, the dissolution kinetics of the different phases may differ greatly, for instance several studies have shown that metallic nickel particles require more aggressive leaching conditions than nickel oxide particles (Larsson et al., 2013; Pietrelli et al., 2005). Determining phase proportions would therefore offer a better understanding of the global leaching kinetics of the elements and thus of the optimal operating conditions. Hence, one of the bottlenecks for efficient hydrometallurgical process design is an in-depth description of BM powders originating from the thermo-mechanical pre-treatment of spent Ni-MH batteries.

To shed light upon this characterization challenge, the main idea of our work is to assess two additional analytical techniques in order to improve BM samples description. These techniques, which are commonly used in mineralogy, are magnetic susceptibility measurements on the one side, and quantitative elemental mapping on the other side.

Magnetic susceptibility (χ) measurements are based on the recording of a magnetic signal whose intensity is proportional to the quantity of ferromagnetic or ferrimagnetic material in a sample (Morales et al., 2016). It is therefore possible to quantify the amount of a given magnetic phase by identifying its Curie temperature in so-called thermomagnetic curves (χ-T curves). Magnetic susceptibility measurements have the advantage of being rapid, non-destructive and low-cost (Hodel et al., 2017; Nédélec et al., 2015).

Quantitative elemental mapping has been widely used in mineralogical studies to describe metamorphic mineral assemblages thanks to the recent improvement of analytical devices such as electron probe μ-analysis (EPMA) (Grammatikopoulos et al., 2011; Lanari et al., 2019; Lanari and Engi, 2017). With prior standardization, the quantitative elemental composition of each pixel on the map can be obtained and statistical analysis allows identification of the types and proportions of phases in the sample. A straightforward approach consists in identifying manually pixels of similar composition, or clusters, from ternary or scatter plots

and rely on in-built mineral databases to classify the clusters into types of phases (Wilson and MacRae, 2005). However, manual identification can introduce human bias and becomes complicated with multi-component and multi-phasic materials such as BM powders.

To produce better-defined multi-dimensional phase maps, several automated classification techniques have been developed, such as the one employed in the software solution XMapTools (Lanari et al., 2014). Automated classification techniques can be divided into either hierarchical or non-hierarchical algorithms. Non-hierarchical clustering algorithms like the *k*-means method are better suited for analysing large data sets, such as maps obtained from rocks and sediments (Carpenter et al., 2014; Maloy and Treiman, 2007; Pownceby et al., 2007). For this reason, only the *k*-means algorithm has been implemented in XMapTools because it is typically used for mineralogical studies. However, it has been shown that the choice of the clustering algorithm can greatly impact the predicted phase proportions (Wilson and MacRae, 2005). For smaller data sets, hierarchical algorithms like Hierarchical Agglomerative Clustering (HAC) are very efficient and could be of use for phase maps processing.

The aim of this study is, therefore, to provide a multi-analytical methodology for characterizing industrial samples of Black Mass (BM) powders originating from cylindrical and prismatic spent Ni-MH batteries. The objectives are (i) to obtain a full elemental mass composition of the powders taking into account not only the metal elements but also carbon and oxygen contents, and (ii) to identify the phases and quantify their relative proportion. The novelty of our research methodology lies in the adaptation of phase-specific analytical techniques used in mineralogy to Ni-MH BM powder characterization: magnetic susceptibility measurements, and EPMA elemental mapping coupled with automated classification techniques built on a homemade MATLAB©-based program implementing several clustering algorithms. Three sieved fractions (0–100 μm, 100–250 μm and 250–600 μm) were considered for the two battery types in order to quantify both the influence of the type of battery and the sieving fraction on the composition of the BM.

2. Materials and methods

2.1. Thermo-mechanical pre-treatment of the batteries

Two industrial samples of cylindrical and prismatic batteries of approximately 600 kg each, were collected and processed separately, according to the method described in our previous work (Zielinski et al. (2020)). The batteries were thermally deactivated in a furnace (300 °C < T < 500 °C) in the absence of exogenous oxygen, leading to an estimated oxygen partial pressure ($PO_{2(g)}$) of about 10^{-30} to 10^{-20} atm. After knife shredding, sieving of the Black Mass powders was carried out in order to obtain three fine fractions of approximately 35 kg for each type of battery: 0–100 μm, 100–250 μm and 250–600 μm. A total of six fractions was thus characterized in this study.

2.2. Characterization of the Black mass powders

2.2.1. Global physicochemical analyses

The samples were characterized for size distribution by laser diffraction using a Malvern MS 3000; the measurements were repeated five times for each sample. The powders were mineralized at 250 °C in aqua regia, and the elemental content of the following elements was determined by ICP-OES (PerkinElmer Optima 8300): Al, Cd, Ce, Co, Cu, Fe, K, La, Li, Mn, Na, Nd, Ni, Pr and Zn. Carbon and oxygen contents were analysed by instrumental gas analysers (IGAs) equipped with IR detectors (EMIA 820 V HORIBA and EMGA 620 W LECO, respectively). The BM fractions were also analysed using powder XRD (D8 BRUKER) in the Θ/2Θ configuration and with Cu Kα radiation (2Θ range of 20 – 80°, λ = 1.5418 Å).

Magnetic susceptibility (χ) was measured as a function of temperature by means of an AGICO KLY-3-CS3 Kappabridge susceptibility meter with an operating frequency of 875 Hz, a magnetic field of 300 Am^{-1} and a sensitivity of 3×10^{-8} SI. Heating and cooling χ–T curves were obtained between 25 °C and 600 °C under Ar atmosphere. Powder samples were weighted on a scale (sensitivity of +/- 1×10^{-4} g) and packed into standard 10 cm^3 tubes. For each sample, two sub-samples were analysed to check for repeatability. Metallic nickel powder (Sigma-Aldrich, 99.7% purity, < 50 μm) was used as a standard for quantifying the amount of metallic nickel in the samples. Uncertainty associated to nickel quantification was calculated by combining the standard uncertainties of the uncorrelated input quantities (mass of the sample powder and bulk susceptibility value).

2.2.2. Quantitative elemental mapping using EPMA

2.2.2.1. Sample preparation and data acquisition. The 0 – 100 μm fraction of the cylindrical batteries was prepared for quantitative elemental mapping using an electron probe μ-analyser (EPMA, CAMECA SXFive, Centre Castaing, Toulouse, France) equipped with 5 wavelength dispersive spectrometers. A cross section of the sample was obtained by embedding the powder in a resin (PolyFast, STRUERS) for hot molding (Mecapress 3, PRESI), diamond-polished down to 1 μm (Mecatech 234, PRESI) and carbon coated to avoid charging effects. A dense and representative area of 765x765 μm^2 was selected. Mapping conditions were 40 nA for the beam current and 15 keV accelerating voltage, a beam diameter of 3 μm, 1 sec dwell time and a pixel size of 3 μm. X-ray intensities of nine elements were measured: Ni, Mn, Co, La, Pr, Nd, Fe, Ce, and O; the choice of these nine representative elements was made according to spot analyses carried out in our previous work on the same sample (Zielinski et al., 2020). A background pass was carried out after each run in order to improve quantitative analysis. Prior to carrying out elemental mapping on the Black Mass sample, point analyses were made on internal standards of know weight concentrations [%wt] corresponding to the nine elements measured during the mapping. More specifically, five point analyses were measured for each standard, which can either be in the form of a pure metal, an alloy or an oxide. Thanks to this analytical standardization, the X-ray intensities of each element could be converted into weight percent concentrations, thus producing a fully quantitative elemental map.

2.2.2.2. Statistical analysis and clustering method. We developed a MATLAB©-based (vR2019) program for the statistical treatment of the elemental map, in order to group pixels of similar compositions into clusters thanks to automated clustering algorithms. The program is structured into two main parts: image processing and clustering algorithms. The image processing part consists in loading the nine compositional matrices [%wt] and a tenth matrix referred to as the 'sum matrix' which corresponds to the sum of the weight concentrations of all the elements for each pixel. In this sum matrix, some pixels have a low value due to several analytical factors: the analysed zone corresponds to the resin in which the sample powder is embedded, a porous particle morphology which decreases the actual electron interaction volume, polishing defaults which do not yield perfectly planar surfaces, or the fact that some elements present in the sample have not been analysed during the mapping. Consequently, the sum matrix was binarized, where the value of 1 was attributed to pixels having a weight concentration greater than 80 %wt. The mask of the reduced sum matrix containing only logical numbers was then applied to the

nine elemental matrices. Finally, the weight concentrations of the nine elemental matrices were normalized.

The second part of the program deals with automated classification algorithms in order to group pixels of similar compositions into clusters. Three classification techniques were implemented, namely the HAC method, the non-hierarchical *k*-means and DBSCAN methods. Clustering results using the three techniques were compared and the HAC method proved to be the most relevant because of its unsupervised nature contrary to the other methods. In the HAC method, a dendrogram is produced that depicts different clustering levels. The similarity of composition of the clusters proposed by the dendrogram was determined by calculating the Calinski-Harabasz index, defined as the ratio of the inter-cluster variance (or the distance in compositional space between the pixels belonging to different clusters) divided by the intra-cluster variance (or the distance in compositional space between the pixels within the same cluster) in the 9-dimensional data set. Therefore, our objective was to maximize this index to find the optimal number of clusters. Once the pixels are attributed to respective clusters, the proportion of each cluster on the mapped zone can be determined by dividing the number of pixels belonging to a given cluster by the total number of pixels contained in the reduced sum matrix. Cluster compositions are first expressed in terms of weight concentrations [%wt], where the median value of each element is reported as well as the interquartile range (IQR) used as an indicator of statistical dispersion. Finally, cluster compositions are converted into molar concentrations [%mol] by normalizing the median weight values of all the elements in each cluster and using respective molar masses to obtain molar concentrations.

2.2.2.3. Phase diagrams calculations. Equilibrium phase diagrams were used as a guide to link the molar compositions of the clusters with mineral phases. $PO_{2(g)}$–T diagrams were plotted within the range of operating conditions of the thermal deactivation step (in the absence of exogenous oxygen $-30 < \log(PO_{2(g)}) < -20$; 300 °C < T < 500 °C) at fixed metal–metal molar ratios, using the FactSage software and the FTOxid database (Bale et al., 2016).

3. Results and discussion

3.1. Particle size distributions

The particle size distributions [%vol] of the three fractions for both battery types are provided in Figure SI-1 and characteristic diameters are detailed in Table SI-1. Although the two battery geometries have a very similar behaviour with respect to sieving, the 0–100 μm and 100–250 μm fractions originating from the prismatic batteries contain slightly finer particles than cylindrical ones. Indeed, for the 0–100 μm fractions, $D_v(50)$ = 18.3 μm for the prismatic batteries (span of 3.77) whereas $D_v(50)$ = 31.8 μm for the cylindrical batteries (span of 2.92); for the 100–250 μm fractions, $D_v(50)$ = 149 μm for the prismatic batteries (span of 1.89) whereas $D_v(50)$ = 166 μm for the cylindrical batteries (span of 1.16). Conversely, the size distribution is almost identical for the 250–600 μm sieved fraction.

3.2. Elemental compositions

Average chemical compositions [%wt] of the six samples obtained from both ICP-OES and IGA are provided in Table 1. A striking observation is that the global nickel content is almost equivalent for all samples, within a close range of 42.4 – 45.0 % wt (Table 1). Oxygen contents are slightly higher for BM powders from prismatic batteries (15.4 – 16.2 %wt) than from cylindrical batteries (13.1 – 14.1 %wt). Other major elements in the BM powders are the light rare earth elements (REEs) La, Ce, Nd and Pr. The total REE content in the samples from cylindrical and prismatic batteries adds up to 14.8 – 15.9 %wt and 11.6 %wt – 17.8 %wt, respectively (Table 1).

Elemental carbon represents a noticeable part of the BM (1.6 – 5.0 %wt). It most likely comes from the residue of organic compounds. The carbon concentrations are comparable to those determined by Ebin et al. (2018) who crushed cylindrical Ni-MH batteries without prior thermal treatment, followed by sieving < 4 mm: for the 0–500 μm fractions, they obtained carbon contents in the range of 1.9 – 4.7 %wt. From a Ni-MH battery recycling process point of view, it is interesting to estimate the carbon content in the BM samples. Indeed, further recycling steps in hydrometallurgical processes require the leaching of BM powders to recover their metal content. However, carbon remains undissolved and causes filtration problems. Therefore, it would be interesting to separate carbon prior to the leaching step not only to facilitate the filtration step, but also because using carbon-free BM powders would improve the throughput of the leaching step. An efficient method for recovering carbon from BM powders could be through flotation techniques, as it was recently proposed by Vanderbruggen and Rudolph (2019) on spent Li-ion batteries (LIBs) BM powders.

The presence of K (2.17 – 4.36 %wt) and Na (<0.57 %wt) in all samples is attributed to residual alkaline electrolyte (Table 1). It should be noted that BM samples from Ni-MH prismatic batteries contain twice as much K than cylindrical batteries, which could indicate that lower electrolyte concentrations are used in cylindrical batteries. We stipulate that traces of Cd and Li (maximal concentrations are 0.83 and 0.13 wt%, respectively) come from cross contamination of the batch of Ni-MH batteries with Ni-Cd and Li-ion batteries during the battery-sorting step.

In all cases, a total mass attribution of more than 92 %wt is obtained; the missing mass can be attributed to additional elements contained in recent Ni-MH battery chemistries (Y, Sm, Zr, Si, Ti, Mg, Sn, V . . .). Altogether, our results demonstrate that within the 0–600 μm sieving range, battery type and size classification have very little influence on the global chemical distribution of the elements in the BM powders.

3.3. Powder XRD analyses

The powder X-Ray diffractograms compiled in Figure SI-2 evidence the presence of Ni, NiO, CeO_2 and graphite as major phases for all the fractions regardless of the battery type. Since the thermal treatment temperature is too low to transform organic compounds into graphite, this type of carbon phase most likely comes from cross contamination during the sorting, crushing and sieving steps at the industrial facilities. The cylindrical batteries (Figure SI-2) a)) also contain a minor phase, the aluminium oxalate $Al_2(C_2O_4)_3$. All spectra feature many other minor peaks (28.34°, 30.57°, 33.93°, 34.26°, 35.10°, 36.31°, 38.66°, 40.64° and 41.10° 2Θ) which could not be indexed. Because of the complexity of the XRD signals and the presence of non-identified peaks, the quantification of the phase repartition using the Rietveld refinement is not possible.

Several expected phases such as the AB_5 mischmetal alloy which could account for abundant elements such as Co and La (Table 1), are not present in our diffractograms. On the other hand, authors who have characterized BM powders obtained from the mechanical treatment of spent Ni-MH batteries, but without prior thermal deactivation (Bertuol et al., 2006; Ebin et al., 2018; Liu et al., 2019) have identified the presence of $Ni(OH)_2$, NiO(OH) and AB_5 mischmetal alloy with powder XRD analyses. The fact that our samples are exempt of these phases indicates that the thermal

Table 1
Chemical composition [%wt] of the 0–100 μm, 100–250 μm and 250–600 μm fractions of the cylindrical-type and prismatic-type batteries obtained from ICP-OES and IGA analyses (DL=detection limit).

Elements	Chemical composition [%wt]					
	Cylindrical-type batteries			Prismatic-type batteries		
	0 – 100 μm	100 – 250 μm	250 – 600 μm	0 – 100 μm	100 – 250 μm	250 – 600 μm
Al	0.85	0.79	0.76	1.03	1.07	1.15
Cd	0.83	0.73	0.55	0.31	0.26	0.12
Co	5.45	4.55	4.62	4.75	3.79	2.42
Cu	0.51	1.16	2.77	0.11	0.15	0.22
Fe	2.90	4.43	4.11	1.21	1.51	1.57
K	2.17	2.40	2.19	4.36	4.25	3.64
Li	0.13	0.11	0.09	0.09	0.08	0.06
Mn	2.37	2.11	2.17	1.97	2.02	2.66
Na	< DL	0.57	0.54	0.36	0.35	0.39
Zn	1.56	1.12	0.96	0.68	0.56	0.41
Ni	44.98	42.40	43.80	44.94	44.48	43.70
La	8.72	8.75	9.11	7.42	8.01	11.79
Ce	5.02	3.86	4.08	2.87	2.99	4.23
Nd	1.68	1.81	1.49	1.05	1.03	1.34
Pr	0.45	0.40	0.42	0.29	0.30	0.42
O	13.1	14.1	13.80	16.20	16.20	15.40
C	2.83	3.20	1.58	5.05	4.42	2.84
Total	93.65	92.50	93.04	92.68	91.49	92.34

pre-treatment induces phase transformations of $Ni(OH)_2$, NiO(OH) and the AB_5 mischmetal alloy.

3.4. Magnetic susceptibility measurements

Heating mass susceptibility curves of the BM samples and their derivatives are plotted in Fig. 2 as a function of temperature (χ–T curves). For each sieving fraction, temperature values of inflexion points are reported in Fig. 2) b) and Fig. 2) d).

The first inflection point for all samples appears at 363 °C on average, which corresponds to the Curie temperature of pure metallic nickel (358 °C) (Legendre and Sghaier, 2011). Using the nickel standard transition peak as a reference and assuming that (i) the analysed volume of the sample powders is the same as that of the standard powder and (ii) the powder densities are relatively equivalent (5.1 $g.cm^{-3}$ for the samples vs. 8.9 $g.cm^{-3}$ for the standard powder), we quantified the amount of metallic nickel in the BM powders. The Hopkinson effect, which corresponds to an increase in magnetic susceptibility between the blocking and Curie temperature of magnetic materials, is present in all curves. However, the potential variations of the Hopkinson effect with respect to grain size or magnetic domain were not taken into account for nickel quantification.

According to the data compiled in Fig. 2) e) the metallic nickel content in cylindrical batteries increases from 2.2 %wt for the 0–100 μm fraction, to 4.4 %wt for the 100–250 μm fraction and up to 6.5 %wt for the 250–600 μm fraction. On the other hand, prismatic batteries contain 4.6 %wt, 9.9 %wt and 12.7 %wt metallic nickel for the 0–100 μm, 100–250 μm and 250–600 μm fractions, respectively. These results illustrate the strong influence of both battery type and fraction size on the content of metallic nickel in the BM samples. For a given fraction, prismatic batteries contain on average twice as much metallic nickel than cylindrical-batteries. Moreover, for each battery type, the 250–600 μm fraction contains three times more metallic nickel than the 0–100 μm fraction, and the 100–250 μm fraction twice as much. The metallic nickel originates from the mesh of the cathode current collector (Larsson et al., 2013). Different fabrication techniques and different behaviour during shredding due to different battery geometries could explain these trends. More specifically, an increasing metallic nickel content with increased sieving fractions could be due to the fact that initial metallic nickel particles are bigger and proportionally less oxidized during pre-treatment. In addition, cathode active mass particles become very brittle after the thermal treatment and easily detachable from the current collector, and would therefore be proportionally more present in the fine fractions. Furthermore, recent work has demonstrated that fibers from the current collectors tend to agglomerate during prolonged sieving, therefore coarser fractions would proportionally contain more agglomerated fibers from the metallic nickel mesh (Porvali et al., 2020). The determination of significant amounts of metallic nickel in the BM samples (2.2 %wt – 12.7 %wt) sheds light on the possible $H_{2(g)}$ explosion risk if degassing is not handled properly during the leaching step.

All fractions from cylindrical batteries exhibit additional magnetic transitions occurring at about 417 °C, 478 °C and 553 °C (Fig. 2) b). The inflection point at 417 °C might be attributed to Ni-Fe-Co alloys. Indeed, according to Pilkington et al. (1964) who studied the magnetic transitions of ternary Ni-Fe-Co alloys, several binary alloys (e.g. 40% mol Ni – 60 %mol Fe alloys and 97% mol Ni – 3 %mol Co) have Curie temperatures close to 400 °C. The inflection point at 478 °C is likely to correspond to the Curie temperature of CeO_2 (467 – 600 °C) (Tiwari et al., 2006). The final transition at around 545 °C is close to Curie temperatures of nickel ferrites Ni_x-$Fe_{3-x}O_4$ with $0 \leq x \leq 1$ (nanocrystalline 517 °C, bulk 570 °C) (Nabiyouni et al., 2010). Broad transition peaks suggest that these solid solutions (nickel ferrites $Ni_xFe_{3-x}O_4$ and Ni-Fe/ Ni-Co alloys) are present within a wide range of chemical composition. Consequently, these phases have not been quantified. The fractions of prismatic batteries (Fig. 2) d), on the other hand, exhibit only distinct magnetic transitions at around 395 °C and 414 °C, which have been attributed to Ni-Fe-Co alloys.

3.5. Elemental mapping analysis

EPMA elemental maps of the nine elements and the sum matrix obtained from a cross section of the 0–100 μm BM powder fraction of cylindrical batteries are detailed in Figure SI-3. The compositional maps were subjected to HAC clustering using our MATLAB©-based program. The dendrogram and corresponding Calinski-Harabasz index evolution with respect to the number of clusters are shown in Fig. 3.

The Calinski-Harabasz index reaches a maximum for a cluster number of 3 (Fig. 3) b); in other words, the ratio between inter-

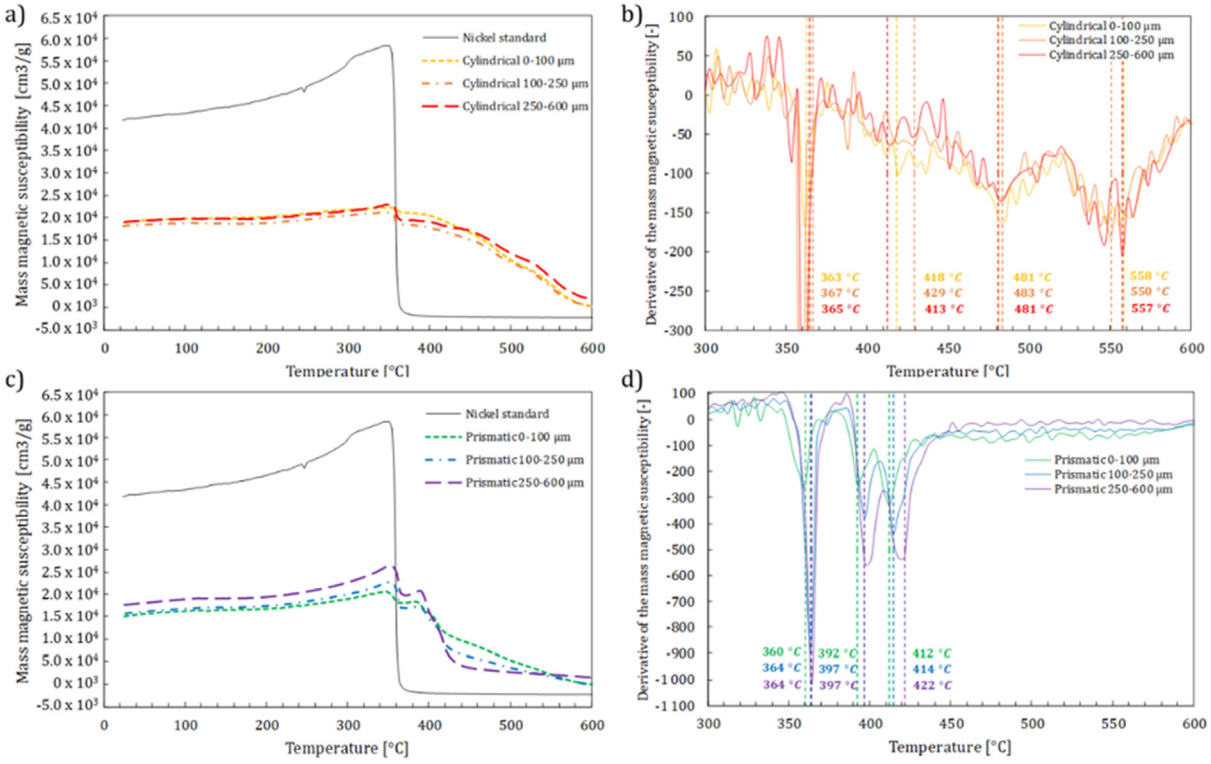

e)

Type of batteries	Metallic nickel content [%wt] of the different fractions		
	0 – 100 µm	100 – 250 µm	250 – 600 µm
Cylindrical	2.16 +/- 0.03	4.41 +/- 0.02	6.50 +/- 0.03
Prismatic	4.63 +/- 0.03	9.86 +/- 0.03	12.66 +/- 0.02

Fig. 2. χ-temperature heating curves for the nickel standard powder and the 0–100 µm, 100–250 µm and 250–600 µm fractions of (a) the cylindrical-type batteries and (b) derivatives of respective heating curves, and of (c) the prismatic-type batteries and (d) derivatives of the respective heating curves; (e) metallic nickel content [%wt] of all the samples calculated from the χ-T heating curves.

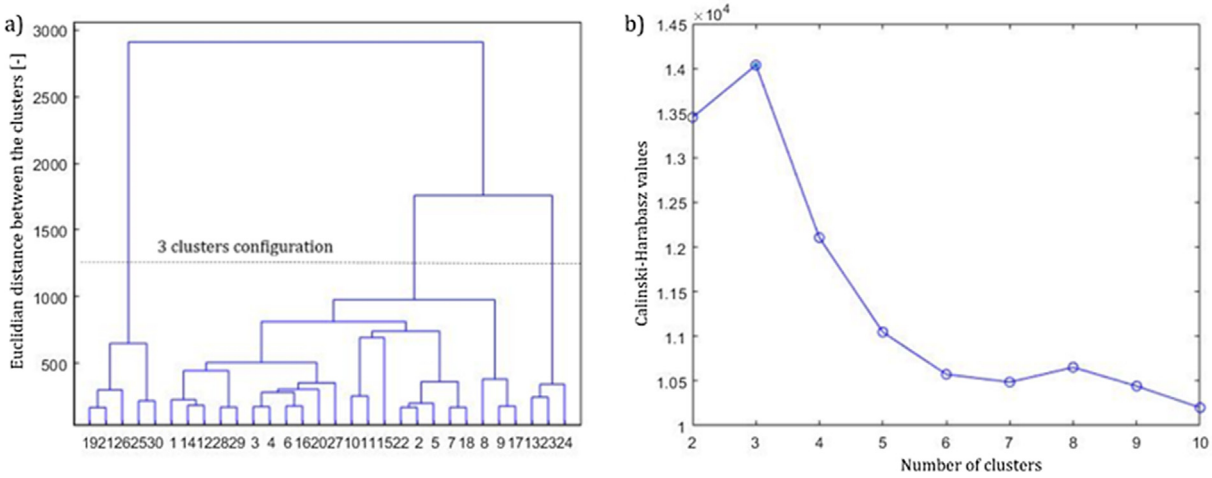

Fig. 3. (a) Dendrogram and (b) corresponding evolution of the Calinski-Harabasz index values with respect to the number of clusters, obtained using the HAC classification method.

cluster variance and intra-cluster variance is the greatest when the number of clusters is 3 so this optimal cluster value was kept for the rest of the analysis. Pixel-cluster attribution in this configuration is depicted in Fig. 4) a). It can be seen that using an 80 %wt threshold on the sum matrix reduces the surface area to 22% of its initial area, which is equivalent to a dense zone of 168 × 168 μm^2 of 14 224 pixels. It should be noted that, since the material is a fine powder embedded in resin, a large part of this discarded area corresponds to resin.

Clustering results expressed in terms of median weight values and IQR [%wt] are reported in Table 2. Moreover, the proportions of the pixels belonging to each cluster are 8.90%, 84.72% and

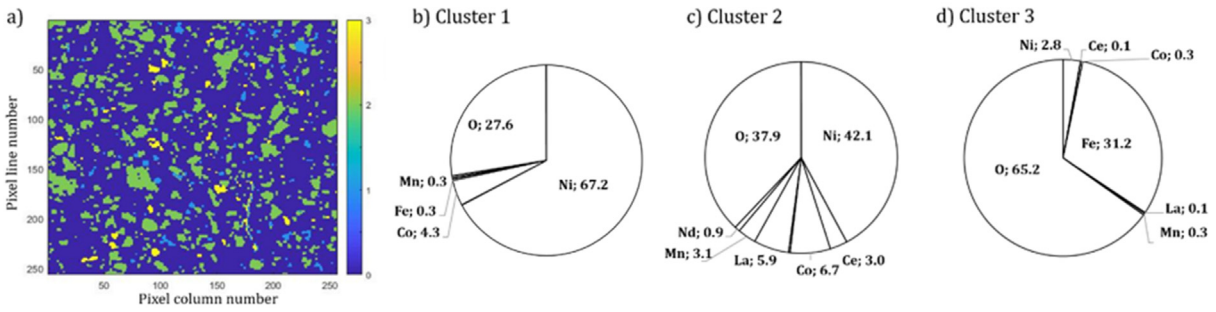

Fig. 4. (a) Pixel-cluster attribution using the HAC classification method, showing the pixels attributed to cluster 1 (blue), cluster 2 (green), cluster 3 (yellow) and the non-considered pixels (purple), and median molar fractions [%mol] of Ni, Ce, Co, Fe, La, Mn, Nd, and O in (b) cluster 1, (c), cluster 2, and (d) cluster 3. (For interpretation of the references to colour in this figure legend, the reader is referred to the web version of this article.)

Table 2
Median weight concentrations [%wt] and inter-quartile range (IQR) [%wt] of the elements in each cluster and corresponding cluster proportions. The equivalent total weight concentration of the elements in the sample [%wt] are recalculated and compared to those obtained by ICP-OES and IGA analyses.

Elements	Chemical composition [%wt] of the clusters using the HAC classification method										Chemical composition [%wt] via ICP-OES and IGA
	Cluster 1			Cluster 2			Cluster 3			Recalculated total weight concentration in the sample [%wt]	
	Median weight concentration [%wt]	IQR [%wt]	Proportion of the cluster [%]	Median weight concentration [%wt]	IQR [%wt]	Proportion of the cluster [%]	Median weight concentration [%wt]	IQR [%wt]	Proportion of the cluster [%]		
Al	–	–	8.90	–	–	84.72	–	–	6.38	–	0.85
Cd	–	–		–	–		–	–		–	0.83
Co	5.40	3.47		7.40	4.00		0.47	0.51		6.78	5.45
Cu	–	–		–	–		–	–		–	0.51
Fe	0.35	0.39		0.32	0.41		57.00	10.30		3.94	2.90
K	–	–		–	–		–	–		–	2.17
Li	–	–		–	–		–	–		–	0.13
Mn	0.36	0.32		3.30	2.85		0.45	0.46		2.86	2.37
Na	–	–		–	–		–	–		–	< DL
Zn	–	–		–	–		–	–		–	1.56
Ni	81.00	7.85		48.00	8.31		5.50	14.73		48.23	44.98
La	0.37	0.38		16.00	9.47		0.56	0.40		13.62	8.72
Ce	0.24	0.26		8.10	4.98		0.29	0.29		6.90	5.02
Nd	0.19	0.19		2.50	2.35		0.22	0.23		2.15	1.68
Pr	0.10	0.23		0.12	0.62		0.00	0.23		0.11	0.45
O	9.10	6.57		12.00	2.80		34.00	6.32		13.14	13.10
C	–	–		–	–		–	–		–	2.83
Total	97.11	–		97.74	–		98.49	–		97.73	93.65

6.38% for cluster 1, cluster 2 and cluster 3, respectively (Table 2). According to the median weight concentrations and cluster proportions, it is possible to recalculate the overall content of each element in the powder. Recalculated values gathered in Table 2 are in very good agreement with those obtained by ICP-OES and IGA on the same sample. Indeed, nickel and oxygen contents recalculated with the clustering data yield values equivalent to those from ICP-OES and IGA; for Ce, Co, Mn, Nd and Fe the overestimation ratio is 1.3 on average. These results confirm that the analysed zone is representative of the overall sample and that the 80 %wt threshold value is adequate. Finally, clusters molar concentration [%mol], recalculated from the median weight concentration of each element per cluster, are shown in Fig. 4.

3.6. Phase composition of the clusters

A thorough discussion based on all the data from the characterization of the 0–100 μm BM powder fraction of the cylindrical batteries is presented in this section. The origin and phase compositions of three groups of particles, referred to as clusters 1 – 3, were evaluated.

3.6.1. Cluster 1

The first cluster is composed of 67.2 %mol Ni, 4.3 %mol Co and 27.6 %mol O as well as traces of Mn and Fe (Fig. 4) b). This leads to a Co/(Ni + Co) molar ratio of 0.06 (Table 3). Given the nickel and oxygen contents, we believe that cluster 1 corresponds to particles coming from (i) the metallic nickel mesh of the cathode current collector that has been partially oxidized during the thermal deactivation and / or shredding steps, and from (ii) the $Ni(OH)_2$ and NiO(OH) cathode active mass particles that have been dehydrated during the thermal treatment. Due to their very close chemical compositions, both types of particles are thus considered as one cluster.

The phase attribution for this cluster is based on two points. Firstly, the dehydration of NiO(OH) occurs in the 100 – 300 °C temperature range and leads to the formation of NiO, as shown for instance by Horanyi (1989). Secondly, according to the P_{O2}-temperature phase diagram of the ternary system Ni-Co-O calculated for Co/(Ni + Co) = 0.06 (Figure SI-4) a) and knowing that the thermal treatment was carried out without exogenous oxygen ($-30 < \log(PO_{2(g)}) < -20$), the stable oxide phase is the monoxide $Ni_{0.94}Co_{0.06}O$. Therefore, the mass balance for cluster 1 leads to a chemical ratio of 0.59 mol of Ni and 0.41 mol of NiO (Table 3),

Table 3
Calculated molar fractions [%mol], molar ratios and phase assemblages for the three clusters.

Elements	Molar fraction in the cluster [%mol]	Molar ratio in the cluster	Phase assemblage of the cluster
Cluster 1			
Ni	62.7	1	$0.59 mol Ni + 0.41 mol NiO$
O	27.6	0.41	
Cluster 2			
M = Ni + Co + Mn	52.0	5.32	$0.35 mol REEs_2O_3 + 0.30 mol CeO_2 + 2.13 mol MO + 3.19 mol M$
O	37.9	3.78	
Ce	3.0	0.30	
REEs = La + Nd + Pr	6.8	0.70	
Cluster 3			
M = Ni + Co + Mn	3.7	1.00	$1 mol M_{0.43}Fe_{2.57}O_4 + 0.54 mol Fe_2O_3$
O	65.2	19.01	
Fe	31.2	8.53	

corresponding to 53.0 %wt of metallic nickel. The proposed transformations for both types of particles in cluster 1 are illustrated in Fig. 5) a) and b).

Multiplying the weight fraction of metallic nickel in the cluster 1 by the overall weight fraction of nickel in the powder as determined by ICP-OES (44.98 %m) and the proportion of pixels belonging to cluster 1 (8.90%) yields a 2.12 %wt of metallic nickel in the sample. This value is equivalent to the amount of metallic nickel obtained by susceptibility measurements (Fig. 2) e). Furthermore, NiO is diamagnetic and was therefore not observable by magnetic susceptibility (Yamaka and Sawamoto, 1958). Finally, the composition of cluster 1 could explain the Ni and NiO peaks identified in the XRD diffractogram (Figure SI-2) a).

3.6.2. Cluster 2

The second cluster consists of 9.8 %mol REEs (with REEs = La, Ce, Nd, Pr), 52.0 %mol M (with M = Ni, Co, Mn) and 37.9 %mol O (Fig. 4) c) corresponding to M/REEs and O/REEs molar ratios of 5.32 and 3.78, respectively (Table 3). A striking observation is that the M/REEs ratio corresponds to the one found in AB_5-type mischmetal particles (with A = La, Ce, Nd and Pr and B = Ni, Co, Mn) (Larsson et al., 2013). As a result, we propose that cluster 2 corresponds to particles coming from the anode active mass that have undergone structural changes due to both Ni-MH battery ageing caused by charge and discharge cycles, as well as the thermal treatment step. As for anode active mass aging, it is well established that lattice expansion and contraction of the alloy during hydrogen absorption and desorption produce mechanical stresses that lead to particle pulverisation (Baërlein et al., 2008; Leblanc et al., 1998). When the anode is cycled in strong alkali electrolyte, smaller particles are generated onto which corrosion scales develop due to solid-state diffusion. Namely, Maurel et al. (2000) have suggested that two corrosion scales develop around the mischmetal core: a layer of rare earth hydroxide needles that are embedded into a continuous mixed subscale of (Ni, Co) solid solution and rare earth hydroxide nanoparticles.

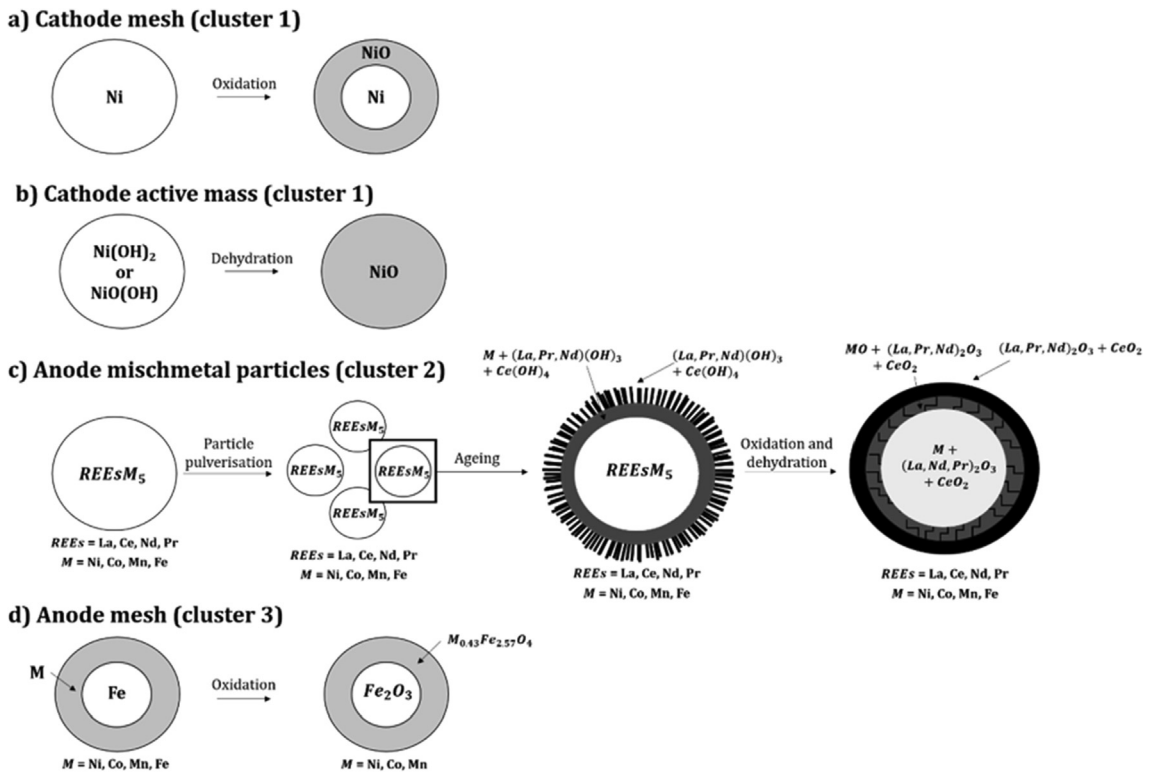

Fig. 5. Proposed phase transformation pathways due to Ni-MH battery ageing mechanisms (particle pulverisation and corrosion during cycling in alkali electrolyte) and the thermal deactivation step, for particles originating from (a) cathode current collector / cluster 1, (b) cathode active mass / cluster 1, (c) anode mischmetal particles / cluster 2, and (d) anode current collector / cluster 3.

Thermal deactivation of the spent Ni-MH batteries is likely to induce further structural changes on the corroded mischmetal particles. The impact of thermal oxidation on BM particle morphology is linked to more recent problematics than those of battery ageing mechanisms, and is therefore poorly documented in the literature. From a thermodynamic approach, the phase diagram of the system Ni-La-O at a fixed La/(Ni + La) molar ratio of 0.16 and $\log(PO_{2(g)})$ < -20 (Figure SI-4) b) indicates that oxidation products are La_2O_3 and NiO. This is confirmed by the works of Blanco et al. (2012), Torresan et al. (2015) and Shirotsuka et al. (1986a, 1986b), who have studied the formation of metal-oxide composites during the thermal degradation of pure $LaNi_5$ in air using differential scanning calorimetry (DSC) from 25 °C to 600 °C. Their results infer that the intermetallic compound is stable up to 140 °C, and then decomposes into successive oxidation steps as shown in Eq. (1) and Eq. (2):

$$2LaNi_5 + \frac{3}{2}O_2 \rightarrow La_2O_3 + 10Ni \quad (1)$$

$$Ni + \frac{1}{2}O_2 \rightarrow NiO \quad (2)$$

According XRD and energy-dispersive X-ray (EDX) analyses of the reaction products, all authors show that La oxidation into La_2O_3 is completed before the formation of NiO due to the strong thermodynamic affinity of REEs for oxygen (Blanco et al., 2012; Torresan et al., 2015). Moreover, Onoe et al. (1988, 1986) have studied the thermal stability of $CeNi_5$ in air within similar temperature ranges and have shown the formation of Ni, NiO and CeO_2 as reaction products.

EPMA spot analyses carried out on this type of particles in our previous study revealed a multiple core–shell structure: a slightly porous outer-shell, a cracked sublayer, and dense unreacted core (Zielinski et al., 2020). We have stipulated that the porous outer-shell comes from the rare earth hydroxide needles that have been oxidized during thermal treatment. Onoe et al. (1986) and Shirotsuka et al. (1986b) have analysed cross-sections of $LaNi_5$ and $CeNi_5$ alloys after oxidation tests, and showed that cracks were only present in the ash layer (La_2O_3 or CeO_2 and NiO) but not in the unreacted core (La_2O_3 or CeO_2 and Ni). We therefore stipulate that the cracked layer observed in our EPMA spot analyses is composed of $(La,Pr,Nd)_2O_3$, CeO_2 and MO (with M = Ni, Co, Mn). Moreover, since no cracks were observed in the dense unreacted core, it was considered to be composed of only $(La,Nd,Pr)_2O_3$, CeO_2 and M (with M = Ni, Co, Mn). The proposed core–shell oxidation mechanism is depicted in Fig. 5) c).

With the hypothesis that REEs are fully oxidized, and for fixed Ce/REEs, M/REEs and O/REEs molar ratios of, respectively, 0.30, 5.32 and 3.78 (Table 3), we obtain the following global phase assemblage for cluster 2: 0.35 mol of $REEs_2O_3$ (with REEs = La, Nd and Pr), 0.30 mol of CeO_2, 2.13 mol of MO and 3.19 mol of M (with M = Ni, Co, Mn). This configuration indicates that 40 %mol of the metallic content in the initial mischmetal particles has been oxidized into a monoxide phase. The remaining metallic content could correspond to the broad peaks attributed to Ni-Co / Ni-Fe alloys on the χ–T curves at around 417 °C (second inflection point in Fig. 2) b) and d). La_2O_3, Nd_2O_3 and Pr_2O_3 are diamagnetic and paramagnetic and can therefore not be quantified using magnetic susceptibility (Sala et al., 2018; Wen et al., 2008). The phase assemblage of cluster 2 is also in good accordance with the CeO_2 phase identified both by magnetic susceptibility and powder XRD (Figure SI-2) a) and Fig. 2) b).

3.6.3. Cluster 3

As can be seen in Fig. 4) d), the third cluster is constituted of 65.2 %mol O, 31.2 %mol Fe and 3.4 %mol M (with M = Ni, Co, Mn. Considering the high iron content, we concluded that particles belonging to cluster 3 come from the nickel-plated steel current collector of the anode which was oxidized during the thermal deactivation step. For a fixed Ni/(Ni + Fe) molar ratio of 0.1 and for $\log(PO_{2(g)})$ < -20, the phase diagram of the system Ni-Fe-O indicates that a nickel ferrite (spinel phase) and hematite Fe_2O_3 should form (Figure SI-2) c). Hypothesizing that Ni, Co and Mn form $(Ni,Co,Mn)_xFe_{3-x}O_4$ with $0 \leq x \leq 1$ and that the remaining iron is fully oxidized into hematite, the phase assemblage which yields Fe/M, O/M and M/(M + Fe) molar ratios relatively equivalent to those found in cluster 3 (namely 8.53, 19.01 and 0.10, respectively) is the following: 1 mol of $M_{0.43}Fe_{2.57}O_4$ and 0.54 mol of Fe_2O_3 (Table 3). The suggested oxidation mechanism is portrayed in Fig. 5) d). This phase assemblage is in agreement with the broad peaks observed on the χ–T curves around 545 °C attributed to nickel ferrites (fourth inflection point in Fig. 2) b)). Hematite is anti-ferromagnetic and has a Neel temperature of 675 °C (Cunha et al., 2017) which is above the maximum temperature used during the susceptibility measurements. However, the presence of Fe_2O_3 could justify the remaining mass magnetic susceptibility of 300 cm^3/g at 600 °C (Fig. 2) b and d).

3.6.4. Extension of the methodology to other types of BM

The proposed phase description of 3 groups of particles is based on the characterization of only one type of BM powder, the 0–100 μm fraction of cylindrical batteries. However, since each phase was attributed to a specific Ni-MH battery component, the number of groups of particles and the nature of the phases identified in each group will be the same regardless of the type of BM powder. On the other hand, we have shown that the proportions of these phases are likely to depend on the type of BM powder, namely due to the fact that bigger particles will be proportionally less oxidized and that different battery geometries behave differently during sieving.

4. Conclusion

The significance of this research lies in the adaptation of phase-specific analytical techniques used in mineralogy, namely magnetic susceptibility measurements and quantitative elemental mapping, to solve urban mining problematics such as the characterisation of industrial samples of spent Ni-MH battery powders. A global comprehension of phase transformation pathways is proposed due both to battery ageing mechanisms and battery thermal deactivation.

Coupling ICP-OES with carbon and oxygen analyses yield total elemental mass attributions greater than 92 %wt for all BM samples. Results demonstrate that the global composition does not depend on the battery type (cylindrical vs. prismatic type batteries) nor on the sieving fraction (0–100 μm, 100–250 μm or 250–600 μm). However, quantitative magnetic susceptibility measurements indicate that the amount of metallic nickel increases when the sieving fraction size is raised, which could infer either that initial metallic nickel particles are bigger and therefore proportionally less oxidized during the thermal deactivation step, and / or that fibers from the metallic nickel mesh agglomerate during sieving and remain in the coarser fractions. Moreover, BM powders from prismatic batteries contain twice as much metallic nickel than cylindrical ones. The metallic nickel content can become significant (up to 13 %wt Ni), which is of high interest for the design and safety of hydrometallurgical recycling processes considering the fact that metallic nickel dissolution produces explosive $H_{2(g)}$ if not handled properly.

Statistical analysis of an EPMA compositional map of a BM powder sample using automated hierarchical clustering algorithms

revealed to be an efficient method for identifying groups of particles and quantifying their proportion. Equilibrium phase diagrams were used as a guide to link the molar compositions of the groups of particles with mineral phases. The main advantage of this technique is that it is easily transferable to all sorts of spent battery BM powders, without the need for prior in-depth knowledge of BM composition.

BM particles were classified into three representative categories, which originate from the partial oxidation of the battery components. The significant amount of oxidized phases in each category highlights the impact of both corrosion mechanisms during charge and discharge cycles of the batteries as well as the battery thermal deactivation step, on the structure and composition of BM particles. This phase proportion determination will later offer a better understanding of the global dissolution kinetics of the elements during the leaching step of BM powders, knowing that dissolution rates can be phase-specific.

Declaration of Competing Interest

The authors declare that they have no known competing financial interests or personal relationships that could have appeared to influence the work reported in this paper.

Acknowledgements

The authors would like to thank Sophie Gouy and Philippe De Parseval from the Centre de Micro-caractérisation Raimond Castaing for the EPMA mapping, Emmanuel Cid from the Laboratoire de Génie Chimique (LGC) for his help with image processing, Loïc Drigo from the laboratory Géosciences Envrionnement Toulouse (GET) for his technical support with the magnetic susceptibility measurements, Laurry Lacombe from the Société Nouvelle d'Affinage des Métaux (SNAM) for the ICP-OES analyses, as well as Cédric Charvillat from the Centre Interuniversitaire de Recherche et d'Ingénierie des Matériaux (CIRIMAT) for the powder XRD measurements. The authors would also like to thank La Région Occitanie for their financial support to this project.

Funding sources

This research received financial support from the Agence Nationale de la Recherche et de la Technologie (ANRT) and La Région Occitanie (project No. 19000678).

Appendix A. Supplementary data

Supplementary data to this article can be found online at https://doi.org/10.1016/j.wasman.2020.09.017.

References

ADEME, 2017. Piles et accumulateurs: rapport anuel 1–146.

Al-thyabat, S., Nakamura, T., Shibata, E., Iizuka, A., 2013. Adaptation of minerals processing operations for lithium-ion (LiBs) and nickel metal hydride (NiMH) batteries recycling: Critical review. Miner. Eng. 45, 4–17. https://doi.org/10.1016/j.mineng.2012.12.005.

Baërlein, P., Antonius, C., Löffler, J., Kümpers, J., 2008. Progress in high-power nickel – metal hydride batteries. J. Power Sources 176, 547–554. https://doi.org/10.1016/j.jpowsour.2007.08.052.

Bale, C.W., Bélisle, E., Chartrand, P., Decterov, S.A., Eriksson, G., Gheribi, A.E., Hack, K., Jung, I.H., Kang, Y.B., Melançon, J., Pelton, A.D., Petersen, S., Robelin, C., Sangster, J., Spencer, P., Van Ende, M.A., 2016. FactSage thermochemical software and databases, 2010–2016. Calphad Comput. Coupling Phase Diagrams Thermochem. 54, 35–53. https://doi.org/10.1016/j.calphad.2016.05.002.

Bernardes, A.M., Espinosa, D.C.R., Tenório, J.A.S., 2004. Recycling of batteries : a review of current processes and technologies. J. Power Sources 130, 291–298. https://doi.org/10.1016/j.jpowsour.2003.12.026.

Bertuol, D., Tenorio, J., Bernardes, A., 2006. Spent NiMH batteries : Characterization and metal recovery through mechanical processing. J. Power Sources 160, 1465–1470. https://doi.org/10.1016/j.jpowsour.2006.02.091.

Blanco, M.V., Zelaya, E., Esquivel, M.R., 2012. Study of the thermal stability in air of LaNi5 by DSC, EDX, TEM and XRD combined techniques. Procedia Mater. Sci. 1, 564–571. https://doi.org/10.1016/j.mspro.2012.06.076.

Carpenter, P.K., Jolliff, B.L., Donovan, J.J., 2014. Compositional mapping by EPMA and μXRF. Microsc. Microanal. 20, 710–711. https://doi.org/10.1017/S1431927614005273.

Chmielarz, A., Becker, K., 2018. Recycling of Ni-MH and Li-ion batteries, in. PROMETIA 5th Scientific Seminar.

Crocce, D., Espinosa, R., Moura, A., Alberto, J., Tenório, S., 2004. An overview on the current processes for the recycling of batteries. J. Power Sources 135, 311–319. https://doi.org/10.1016/j.jpowsour.2004.03.083.

Cunha, A.A., Da Silva, F.L., Silva, B.M.C., Mendes, J.J., Solé, R.A.L., Da Silva Araújo, F.G., 2017. Thermomagnetic study for identification of mineral phases. Mater. Res. 20, 125–129. https://doi.org/10.1590/1980-5373-mr-2017-0044.

Ebin, B., Petranikova, M., Ekberg, C., 2018. Physical separation, mechanical enrichment and recycling-oriented characterization of spent NiMH batteries. J. Mater. Cycles Waste Manag. https://doi.org/10.1007/s10163-018-0751-4.

Grammatikopoulos, T., Mercer, W., Gunning, C., Prout, S., 2011. Quantitative characterization of the REE minerals by QEMSCAN from the Nechalacho Heavy Rare Earth Deposit, Thor Lake Project, NWT, Canada. Proc. 43rd Annu. Can. Miner. Process. Conf. 381–398.

Hall, D.S., Lockwood, D.J., Bock, C., Macdougall, B.R., Lockwood, D.J., 2014. Nickel hydroxides and related materials: a review of their structures, synthesis and properties. Royal Society.

Hodel, F., Macouin, M., Triantafyllou, A., Carlut, J., Berger, J., Rousse, S., Ennih, N., Trindade, R.I.F., 2017. Unusual massive magnetite veins and highly altered Cr-spinels as relics of a Cl-rich acidic hydrothermal event in Neoproterozoic serpentinites (Bou Azzer ophiolite, Anti-Atlas, Morocco). Precambrian Res. 300, 151–167. https://doi.org/10.1016/j.precamres.2017.08.005.

Horanyi, T.S., 1989. The thermal stability of β-Ni(OH)2-β-NiOOH system. Thermochim. Acta 137, 247–253.

Huang, K., Li, J., Xu, Z., 2011. Enhancement of the recycling of waste Ni-Cd and Ni-MH batteries by mechanical treatment. Waste Manag. 31, 1292–1299. https://doi.org/10.1016/j.wasman.2011.01.006.

Innocenzi, V., Vegliò, F., 2012. Recovery of rare earths and base metals from spent nickel-metal hydride batteries by sequential sulphuric acid leaching and selective precipitations. J. Power Sources 211, 184–191. https://doi.org/10.1016/j.jpowsour.2012.03.064.

Lanari, P., Engi, M., 2017. Local bulk composition effects on metamorphic mineral assemblages. Rev. Mineral. Geochem. 83, 55–102.

Lanari, P., Vho, A., Bovay, T., Airaghi, L., Centrella, S., 2019. Quantitative compositional mapping of mineral phases by electron probe micro-analyser. Geol. Soc. Spec. Publ. 478, 39–63. https://doi.org/10.1144/SP478.4.

Lanari, P., Vidal, O., De Andrade, V., Dubacq, B., Lewin, E., Grosch, E.G., Schwartz, S., 2014. XMapTools: A MATLAB©-based program for electron microprobe X-ray image processing and geothermobarometry. Comput. Geosci. 62, 227–240. https://doi.org/10.1016/j.cageo.2013.08.010.

Larsson, K., Ekberg, C., Ødegaard-Jensen, A., 2013. Dissolution and characterization of HEV NiMH batteries. Waste Manag. 33, 689–698. https://doi.org/10.1016/j.wasman.2012.06.001.

Leblanc, P., Knosp, B., Jordy, C., Blanchard, P., 1998. Mechanism of alloy corrosion and consequences on sealed nickel-metal hydride battery performance. J. Electrochem. Soc. 145, 860–863.

Legendre, B., Sghaier, M., 2011. Curie temperature of nickel. J. Therm. Anal. Calorim. 105, 141–143. https://doi.org/10.1007/s10973-011-1448-2.

Liu, F., Peng, C., Porvali, A., Wang, Z., Wilson, B., Lundström, M., 2019. Synergestic recovery of valuable metals from spent NiMH and Li-ion batteries. ACS Sustain. Chem, Eng.

Maloy, A.K., Treiman, A.H., 2007. Evaluation of image classification routines for determining modal mineralogy of rocks from X-ray maps. Am. Mineral. 92, 1781–1788.

Maurel, F., Knosp, B., Backhaus-Ricoult, M., 2000. Characterization of Corrosion Products of AB 5 -Type Hydrogen Storage Alloys for Nickel-Metal Hydride Batteries. J. Electrochem. Soc. 147, 78–86.

Morales, J., Hernandez-Bernal, M. del S., Corona-Chavez, P., Gogichaishvili, A., Bautista, F., 2016. Further evidence for magnetic susceptibility as a proxy for the evaluation of heavy metals in mining wastes: case study of Tlalpujahua and El Oro Mining Districts. Environ. Earth Sci. 75. https://doi.org/10.1007/s12665-015-5187-8.

Nabiyouni, G., Fesharaki, M.J., Mozafari, M., Amighian, J., 2010. Characterization and magnetic properties of nickel ferrite nanoparticles prepared by ball milling technique. Chinese Phys. Lett. 27, 6–9. https://doi.org/10.1088/0256-307X/27/12/126401.

Nédélec, A., Trindade, R., Peschler, A., Archanjo, C., Macouin, M., Poitrasson, F., Bouchez, J.L., 2015. Hydrothermally-induced changes in mineralogy and magnetic properties of oxidized A-type granites. Lithos 212–215, 145–157. https://doi.org/10.1016/j.lithos.2014.11.007.

Onoe, K., Furukawa, N., Shirotsuka, T., 1988. Comparison of catalytic properties of Ni/CeO2 and Ni/La2O3 prepared by low-temperature oxidation. Procedia Mater. Sci. 21, 451–456.

Onoe, K., Shirotsuka, T., Yokoyama, A., 1986. Effect of oxidation conditions on Ni crystallite size in preparation of catalysts from rare earth intermetallic compounds. J. Chem. Eng. Japan 19, 347–349.

Pietrelli, L., Bellomo, B., Fontana, D., Montereali, M., 2005. Characterization and leaching of NiCd and NiMH spent batteries for the recovery of metals. Waste Manag. 25, 221–226. https://doi.org/10.1016/j.wasman.2004.12.013.

Pilkington, T.C., Artley, J.L., Wooten, F.T., 1964. Prediction of Curie temperatures in ternary Fe-Co-Ni alloys. J. Appl, Phys, p. 33.

Porvali, A., Ojanen, S., Wilson, B.P., Serna-Guerrero, R., Lundström, M., 2020. Nickel Metal Hydride Battery Waste: Mechano-hydrometallurgical Experimental Study on Recycling Aspects. J. Sustain. Metall. 6, 78–90. https://doi.org/10.1007/s40831-019-00258-2.

Pownceby, M.I., MacRae, C.M., Wilson, N.C., 2007. Mineral characterisation by EPMA mapping. Miner. Eng. 20, 444–451. https://doi.org/10.1016/j.mineng.2006.10.014.

Sala, G., Stone, M.B., Rai, B.K., May, A.F., Cruz, C.R. Dela, Arachchige, H.S., Ehlers, G., Fanelli, V.R., Garlea, V.O., Lumsden, M.D., Mandrus, D., Christianson, A.D., 2018. Physical properties of the trigonal binary compound Nd2O3. Phys. Rev. Mater. 2. https://doi.org/10.1103/PhysRevMaterials.2.114407.

Shirotsuka, T., Onoe, K., Yokoyama, A., 1986a. The influence of preparation variables on ni crystallite size in high temperature oxidation of LaNi5 accompanied by an increase in surface area. J. Chem. Eng. Japan 19, 519–523. https://doi.org/10.1252/jcej.19.519.

Shirotsuka, T., Onoe, K., Yokoyama, A., 1986b. Effects of oxidation of LaNi5 on Ni dispersion. J. Chem. Eng. Japan 19, 91–95. https://doi.org/10.1252/jcej.19.91.

Tiwari, A., Bhosle, V.M., Ramachandran, S., Sudhakar, N., Narayan, J., Budak, S., Gupta, A., 2006. Ferromagnetism in Co doped CeO 2: Observation of a giant magnetic moment with a high Curie temperature. Appl. Phys. Lett. 88, 93–96. https://doi.org/10.1063/1.2193431.

Torresan, F., Mogni, L.V., Esquivel, M.R., 2015. Metal/oxide composites: mechanisms of the formation from the thermal decomposition of LaNi5. Procedia Mater. Sci. 8, 1108–1117. https://doi.org/10.1016/j.mspro.2015.04.174.

Vanderbruggen, A., Rudolph, M., 2019. Flotation of spherodized graphite from spent Lithium Ion Batteries, in: MEI Flotation'19. https://doi.org/10.13140/RG.2.2.19222.09281.

Wang, H., Friedrich, B., 2015. Development of a highly efficient hydrometallurgical recycling process for automotive Li-ion batteries. J. Sustain. Metall. 168–178. https://doi.org/10.1007/s40831-015-0016-6.

Wen, Q., Zhang, H., Song, Y., Yang, Q., Zhu, H., Wang, W., Xiao, J.Q., 2008. Room-temperature ferromagnetism in Co doped La2O3. J. Appl. Phys. 103. https://doi.org/10.1063/1.2830072.

Wilson, N.C., MacRae, C.M., 2005. An automated hybrid clustering technique applied to spectral data sets. Microsc. Microanal. 11, 434–435. https://doi.org/10.1017/s1431927605501168.

Yamaka, E., Sawamoto, K., 1958. Electrical conductivity of NiO near the curie temperature. Phys. Rev. 112, 1861–1862. https://doi.org/10.1103/PhysRev.112.1861.

Zielinski, M., Cassayre, L., Destrac, P., Coppey, N., Garin, G., Biscans, B., 2020. Leaching mechanisms of industrial powders of spent nickel metal hydride batteries in a pilot-scale reactor. ChemSusChem 4, 616–628. https://doi.org/10.1002/cssc.201902640.

Supplementary Interactive Plot Data (CSV)

Supporting Information

A multi-analytical methodology for the characterization of industrial samples of spent Ni-MH battery powders

Margot Zielinski[1,2], Laurent Cassayre[1], Pascal Floquet[1], Mélina Macouin[3], Philippe Destrac[1], Nicolas Coppey[2], Cédric Foulet[2], and Béatrice Biscans[1,*]

[1] Laboratoire de Génie Chimique, Université de Toulouse, CNRS, INPT, UPS, Toulouse, France
[2] Société Nouvelle d'Affinage des Métaux (S.N.A.M.), Viviez, France
[3] GET/OMP, UMR CNRS 5563, Université Paul-Sabatier, Toulouse, France

*Corresponding author: beatrice.biscans@toulouse-inp.fr

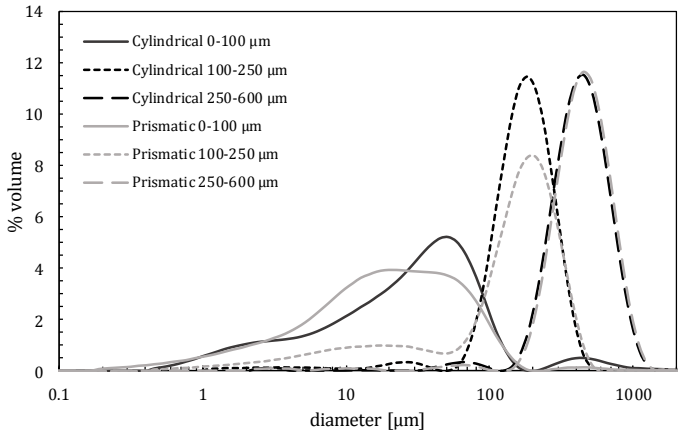

Figure SI-1 Particle size distribution [%vol] of the 0-100 µm, 100-250 µm and 250-600 µm fractions obtained from the cylindrical-type and prismatic-type batteries

Type of battery	Sieved fraction	Dv(10) [µm]	Dv(50) [µm]	Dv(90) [µm]	Span
	0-100 µm	3.15	31.8	95.9	2.92
Cylindrical	100-250 µm	89.9	166	283	1.16
	250-600 µm	227	405	694	1.15
	0-100 µm	2.52	18.3	71.6	3.77
Prismatic	100-250 µm	9.96	149	292	1.89
	250-600 µm	239	423	721	1.14

Table SI-1 Dv(10), Dv(50) and Dv(90) and spans of the 0-100 µm, 100-250 µm and 250-600 µm fractions of the cylindrical-type and prismatic-type battery BM powders

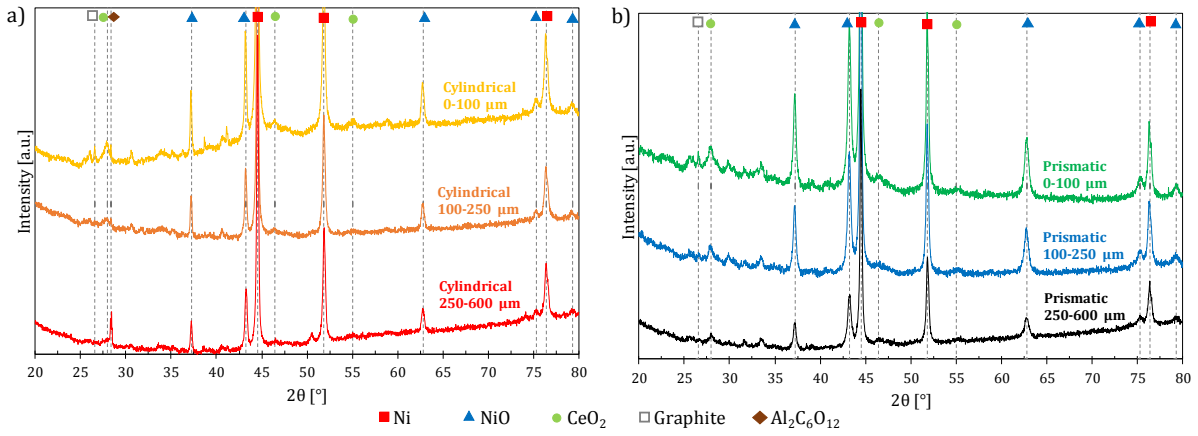

Figure SI-2 Powder XRD analysis of the 0-100 µm, 100-250 µm and 250-600 µm fraction for the (a) cylindrical-type type batteries and (b) prismatic-type batteries

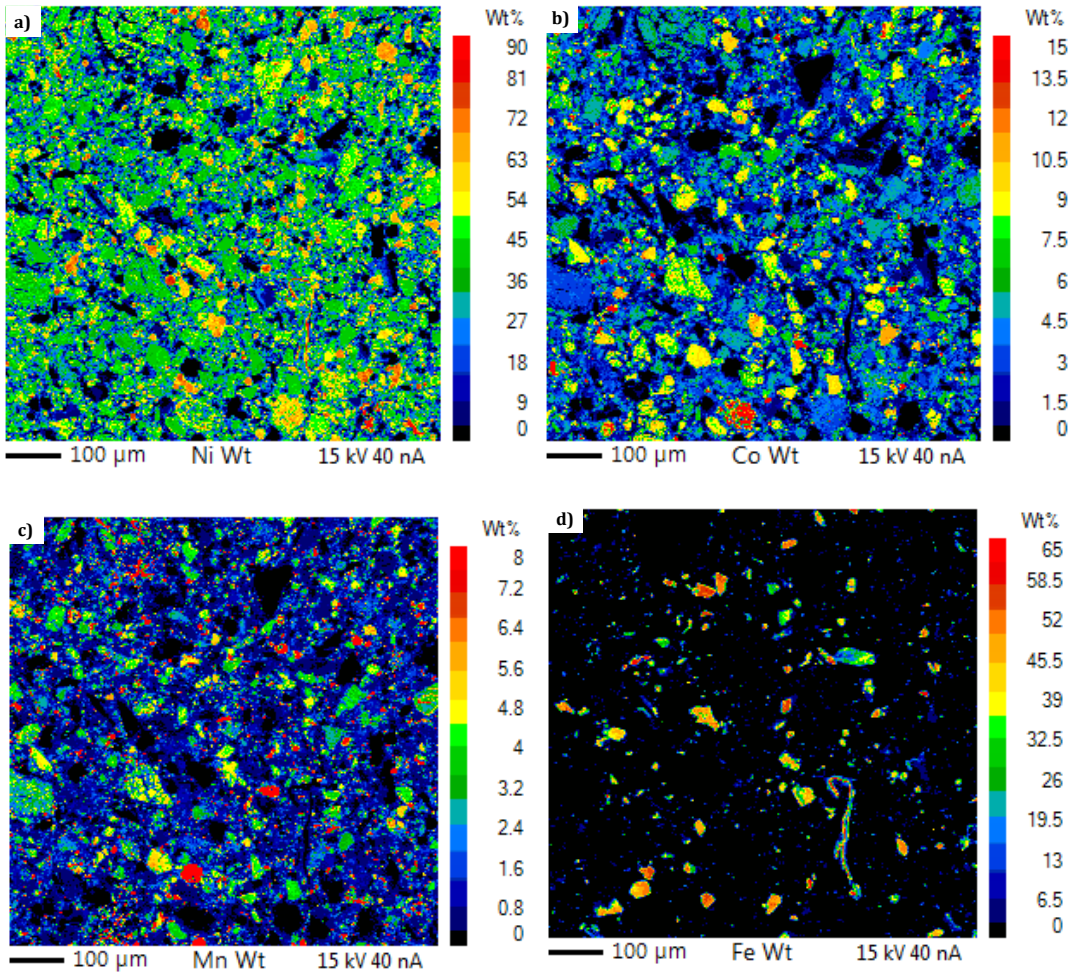

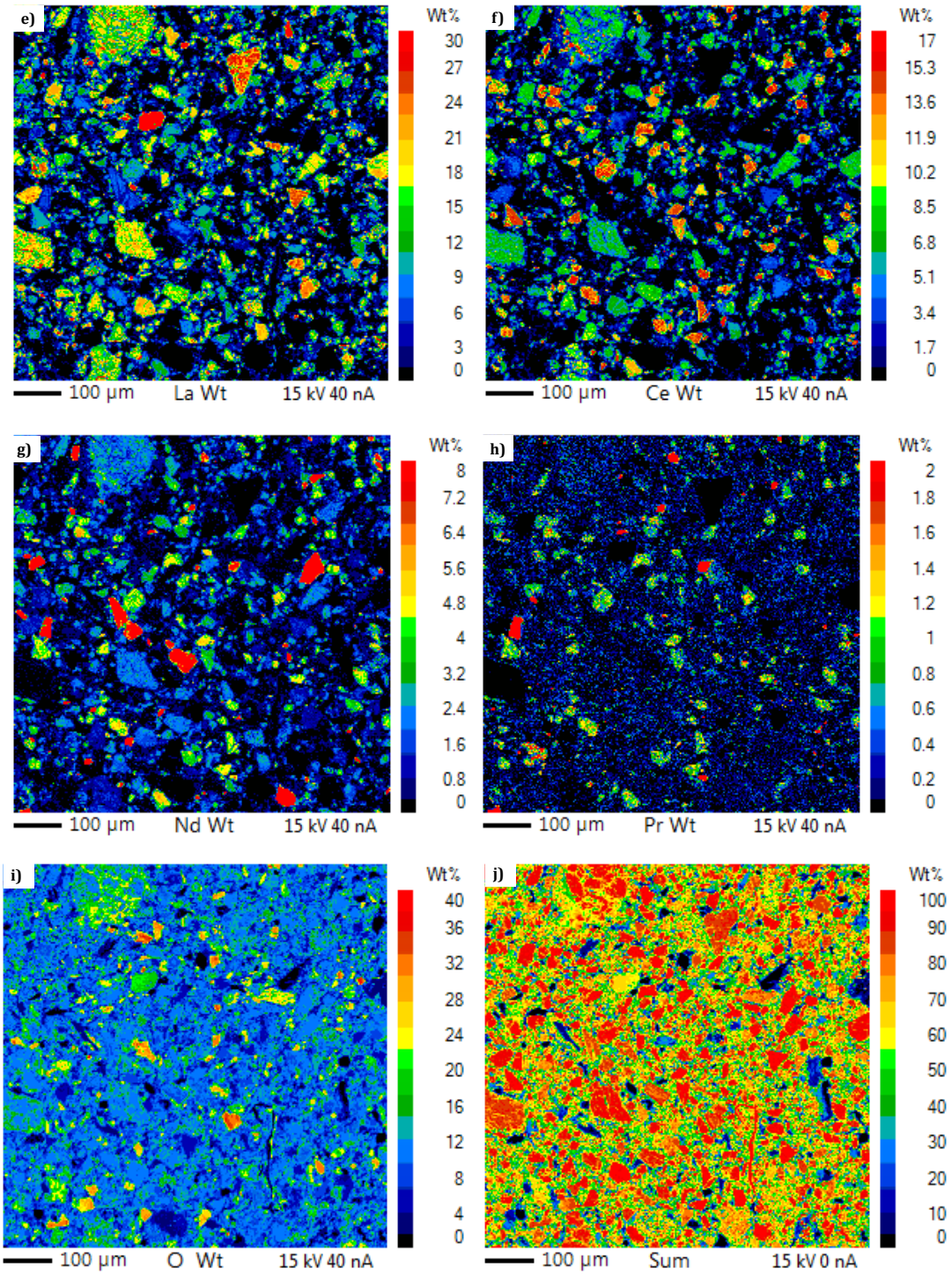

Figure SI-3 EPMA elemental maps [%wt] of (a) Ni, (b) Co, (c) Mn, (d) Fe, (e) La, (f) Ce, (g) Nd, (h) Pr, (i) O, and (j) the sum matrix.

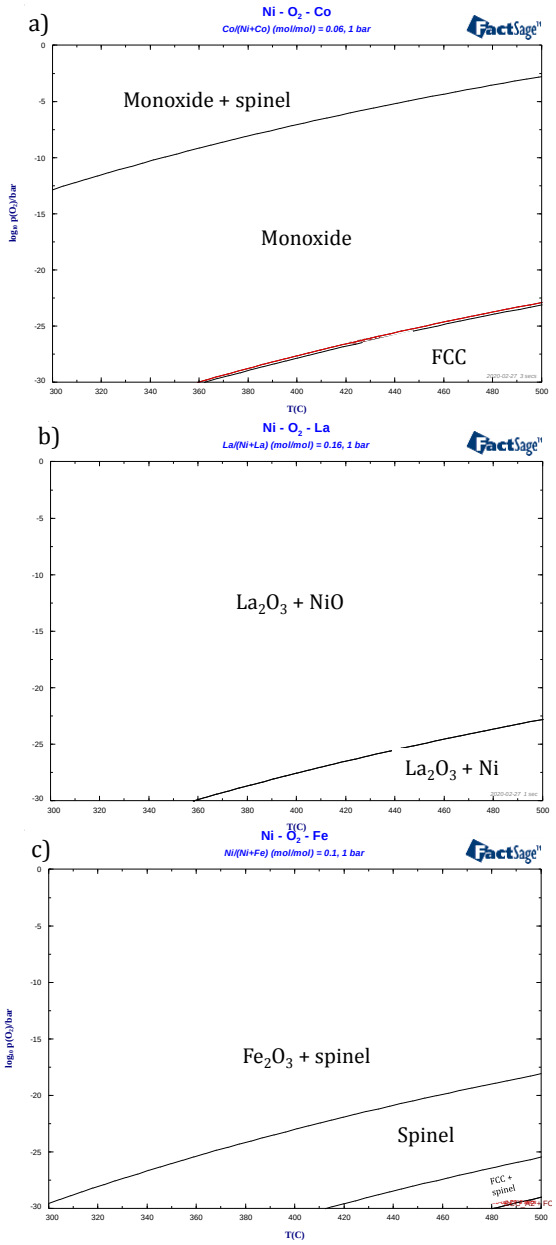

Figure SI-4 Calculated equilibrium phase diagrams for the ternary systems (a) Ni-Co-O with a fixed Co/(Ni+Co) molar ratio of 0.06, (b) Ni-La-O with a fixed La/(Ni+La) molar ratio of 0.16, and (c) Ni-Fe-O with a fixed Ni/(Ni+Fe) molar ratio of 0.1, for -30 bar < $\log(PO_{2(g)})$ < 0 and 300°C < T < 500°C